HIGH-RESOLUTION LUNAR TOPOGRAPHY FROM PHOTOGRAPHIC DATA AND LASER ALTIMETRY

Iris Fernandes, Klaus Mosegaard
Niels Bohr Institute
University of Copenhagen

ABSTRACT

Mapping landforms on the Moon is of great interest and importance for future human settlements and resources exploration. One of the first steps is to map the topography and investigate their shape and geometry in great detail and resolution, which would provide the first conditions for assessing their suitability for future on-site analysis. However, data from the Lunar Orbiter Laser Altimeter (LOLA) provide low resolution elevation maps in comparison to the size of detailed geological features. To improve resolution, we developed an inverse method to upscale topographic maps to a higher resolution using photographic data from the Lunar Reconnaissance Orbiter Camera (LROC). The method, which exploits the relation between topographic gradients and degrees of shading of incoming sunlight, shows an improvement from ~60 metres per pixel to 0.9 metres per pixel, bringing it to the same resolution as the optical images from LROC. Our method can detect craters as small as ~3 metres of diameter and, if illumination from several angles are available, is potentially a way to remove shades from complex features such as caves. It is also possible to estimate the error of the model due to uncertainties in the albedo.

Keywords: planetary physics, planetary exploration, error estimation, surface mapping, computational modelling, applied geophysics, Moon surface, lunar landforms, space science, LOLA

INTRODUCTION

Surveying Lunar landforms is often challenging, presenting several technical obstacles in terms of engineering, data and image processing, computational power and mathematical complexity. Interesting features are observed from the Lunar Reconnaissance Orbiter Camera (LROC) in photographic optical images in Regions of Interest (ROI) such as caves, lava tube pits, lava channels and craters under shaded areas, possibly containing water ice (Smith, D. E. et all, 1997; Smith, D. E. et all, 2010(1); Smith, D. E. et all, 2010(2)).

Mapping these areas is fundamental for any further investigation supporting the decision making in connection with future human settlements and resources exploration. For this, it is necessary to identify the surface geology, the rock composition and its spatial distribution, and similarities with Earth or other planetary bodies, to infer the possibility of accessing ISRU (In-Situ Resource Utilization) (Johnson et all., 2010).

One of the initial stages is to map the topography and probe geological features of the landforms. All this would only be possible if the imagery data contains enough detail and resolution; poor resolution means missing important and small elements, for instance cave entrances and lava tubes.

Imagery data by NASA space craft, the Lunar Reconnaissance Orbiter Camera (LROC), provides optical photos showing images in scale of approximately half to one metre per pixels. However, the original topographic data acquired by the Lunar Orbiter Laser Altimeter (LOLA) onboard LRO provided elevation maps of approximately 60 metres per pixel near the equator. This poorer resolution in comparison with the photos misses smaller surface elements, thereby increasing the uncertainty of geological interpretations.

The challenge of retrieving important small-scale features in planetary bodies has being a subject of several studies for decades. In a NASA report carried out by William Whittaker (2012), methodologies are discussed for developing high resolution modelling of surface and subsurface phase-I lunar mapping with sparse data, enabling robotic phase-II developments. In part of this research, a simulated area was created to imitate the view of landers or rovers - which means in higher resolution. This method shows a synthetic case where a low-resolution terrain was used and then added new small features in accordance to statistical models of Surveyor data (NASA Surveyor Project Final Report, 1968). A photo was created from this reconstructed LiDAR map. Due to the complexity of these studies it is necessary to develop elaborated robotic missions. In this same report, it is described how rovers and landers equipped with LiDAR cameras and small gadgets will be taken to lava pit entrances to investigate their interior. In this way, a series of robotic missions are made necessary to compensate for the lack of information we have from orbit in phase I.

A different approach carried by Kaku, T. et all (2017) is about mapping the lunar cave Marius Hills, whose diameter is approximately 65 metres (Haruyama, J. et al., 2009). Using SELENE Lunar Radar Sounder (LRS) they developed a technique combining LRS patterns with gravity data, showing regions with lower gravity suggesting the presence of voids, for instance, lava tubes or caves. Also, as seen in Haruyana J., et all 2012(1) and Haruyana J., et all 2012(2) SELENE data has been used to create Lunar Digital Terrain Models from terrain stereo camera observations.

Also, in an attempt to improve the resolution of small geological features, a study carried out by Barker, M.K. et al. (2015) offers improved lunar digital elevation models (DEM) considering geo-location errors. This method uses the SELENE Terrain Camera data as constraints to remove errors in orbital pointing and positioning from topographic data from LOLA, by filling gaps in the topographic data using the TC data without the need of interpolation. Although this method is robust and presents an excellent alternative for improving DEM's, the resolution of 512 pixels per degree from LOLA data (~60m per pixel) is maintained and the resolution of the Terrain Camera photos are down-scaled to match the topographic resolution.

In a recent, important work from Barker, M.K. et al. (2021), a DEM in higher resolution from the LOLA-based model is presented where only laser altimetry is used to consistently reduce orbital errors. This method provides 5 metres per pixel resolution.

To contribute to improvement of remote exploration methods, we developed a new theoretical and numerical approach to compute high-resolution topography from photographic data, constrained by lower-resolution altimetry data. We use an inverse problem formulation based on Tarantola and Valette (1982) and Tarantola (2005) where the solar illumination

and albedo is linked to the photographic brightness, which in turn provides information about the slopes of the terrain. Gradients can be calculated and, in combination with low-resolution altimetry data, can be used to reconstruct the high-resolution topography.

The results show a significant improvement of the elevation resolution from the aforementioned 60 metres to the less than one metre (same as the photos) per pixel. To perform the inverse problems calculations, we assumed a constant albedo everywhere, but the resulting uncertainties were subsequently quantified and presented along with the results.

In the theory section we derive the equations and explain in detail the theoretical approach that was developed. In the numerical methods section, we present a computational experiment in a synthetically created area to test our mathematical formulation as well as the algorithm. Finally, in the results section we apply it to real data from the Moon.

THEORETICAL FORMULATION

We use an inverse problems approach (Tarantola, 2005) to find the maximum a posteriori model of the high-resolution topography. Let us define the desired high-resolution topography map (matrix) $\boldsymbol{M}$, and the gradient maps $\boldsymbol{X}$ and $\boldsymbol{Y}$, providing information about the slopes from the illumination in North-South and East-West direction, respectively. The matrix $\boldsymbol{G}$ is the topography gradient operator (NS direction) and $\boldsymbol{G}'$ its transposed (the gradient operator in the EW direction).

Linear Least Squares Inversion of high-resolution photographic brightness data, constrained on low-resolution altimetry data

We wish to solve the linear least squares inverse problem for the unknown high-resolution topographic image model $\boldsymbol{M}$. Here we use the gradients derived from the photographic data as constraints:

$$\boldsymbol{GM} = \boldsymbol{X}$$
$$\boldsymbol{MG}' = \boldsymbol{Y}$$

To constrain our estimate of the high-resolution topography, we assume that the LOLA low resolution data is an down-sampled version of $\boldsymbol{M}$. We do this by using the LOLA low resolution topography $\boldsymbol{M}_0$ as our prior model and define the "model update" $\Delta\boldsymbol{M} = \boldsymbol{M} - \boldsymbol{M}_0$. If $\boldsymbol{X}_0$ and $\boldsymbol{Y}_0$ are rough estimates of the gradients calculated directly from the LOLA low resolution topography, we can also define "data residuals" $\Delta\boldsymbol{X} = \boldsymbol{X} - \boldsymbol{X}_0$ and $\Delta\boldsymbol{Y} = \boldsymbol{Y} - \boldsymbol{Y}_0$, and since

$$\boldsymbol{GM}_0 = \boldsymbol{X}_0$$
$$\boldsymbol{M}_0\boldsymbol{G}' = \boldsymbol{Y}_0$$

we can formulate equations for the updates:

$$\boldsymbol{G}\Delta\boldsymbol{M} = \Delta\boldsymbol{X}$$
$$\Delta\boldsymbol{M}\boldsymbol{G}' = \Delta\boldsymbol{Y}. \qquad (1)$$

Once the updates are found, we can compute the high-resolution topography estimate as

$$\boldsymbol{M} = \Delta\boldsymbol{M} + \boldsymbol{M}_0.$$

As input to these calculations, $\boldsymbol{M}_0$, $\boldsymbol{X}_0$ and $\boldsymbol{Y}_0$ are available from the LOLA data, but we need to estimate the full gradients $\boldsymbol{X}$ and $\boldsymbol{Y}$ to obtain $\Delta\boldsymbol{X}$ and $\Delta\boldsymbol{Y}$. The components of these gradients matrices are the local gradients of the topography $f(x, y)$ and they are related to the normal vector $\boldsymbol{N}(x, y)$ through:

$$\boldsymbol{N}(x,y) = \begin{pmatrix} \frac{\partial f}{\partial x}(x,y) \\ \frac{\partial f}{\partial y}(x,y) \\ -1 \end{pmatrix},$$

giving a *unit* normal vector

$$\boldsymbol{n}(x,y) = \frac{\boldsymbol{N}(x,y)}{|\boldsymbol{N}(x,y)|}.$$

If the surface at is hit by light with unit direction vector $\boldsymbol{s}$, the illumination damping factor δ is the magnitude of the projection of $\boldsymbol{s}$ on $\boldsymbol{n}(x,y)$, scaled by the albedo a:

$$\delta(x,y) = a\,\boldsymbol{s}\cdot\boldsymbol{n}(x,y)$$

giving 1 when $\boldsymbol{n}(x,y)$ and $\boldsymbol{s}$ are parallel, and 0 when $\boldsymbol{n}(x,y)$ and $\boldsymbol{s}$ are perpendicular. If we know $\boldsymbol{s}$, and have an estimate of the albedo ($a \approx 0.12$ for the Moon), then we can get the damping factor (brightness) $\delta(x,y)$ from the photographic data. We can now compute a least squares estimate of $\boldsymbol{n}(x,y)$,

$$\boldsymbol{n} = \boldsymbol{n}_0 + \boldsymbol{D^T}(\boldsymbol{DD^T} + \boldsymbol{\epsilon^2 I})^{-1}(\delta - \delta_0)$$

where $\boldsymbol{D}$ is the dot product (and scaling) operator, defined by $\boldsymbol{Dv} = a\,\boldsymbol{s}\cdot\boldsymbol{v}$, ϵ is a regularization parameter, $\boldsymbol{n}_0$ and δ_0 are a priori estimates of the normal vector and the brightness, respectively, computed directly from the low resolution LOLA topography. From $\boldsymbol{n}$ we can get the required gradients.
To finally solve (1) for $\Delta\boldsymbol{M}$, we need to simultaneously minimize the difference between the left-hand and the right-hand sides of these equations. That is, we need to minimize the following expression with respect to $\Delta\boldsymbol{M}$:

$$\sigma_D^{-2}\|\boldsymbol{G}\Delta\boldsymbol{M} - \Delta\boldsymbol{X}\|^2 + \sigma_D^{-2}\|\Delta\boldsymbol{M}\boldsymbol{G}' - \Delta\boldsymbol{Y}\|^2 + \sigma_M^{-2}\Delta\boldsymbol{M} \quad (2)$$

where σ_D^2 is the variance of the noise on the data, and σ_M^2 is the a priori variance of the unknown model $\boldsymbol{M}$.

It can be shown (see Appendix) that, for any matrices $\boldsymbol{A}, \boldsymbol{B}$ and $\boldsymbol{C}$ with appropriate dimensions, the derivative of the error expression:

$$E(\boldsymbol{\mathcal{M}}) = \|\boldsymbol{A\mathcal{M}B} - \boldsymbol{C}\|^2$$

with respect to the components of a matrix $\boldsymbol{\mathcal{M}}$ are:

$$\left\{\frac{\partial E_D}{\partial \boldsymbol{\mathcal{M}}_{pq}}\right\} = 2\boldsymbol{A'A\mathcal{M}B'B} - 2\boldsymbol{A'CB}\,.$$

Using this result for $\boldsymbol{\mathcal{M}} = \Delta\boldsymbol{M}$ we can now minimize expression (2) through differentiation and setting equal to zero:

$$\sigma_D^{-2}(\boldsymbol{G'G}\Delta\boldsymbol{M} - \boldsymbol{G'X} + \Delta\boldsymbol{M}\boldsymbol{G'G} - \boldsymbol{YG}) + \sigma_M^{-2}\Delta\boldsymbol{M} = \boldsymbol{0}$$

or,

$$\sigma_D^{-2}(\boldsymbol{G'G}\Delta\boldsymbol{M} + \Delta\boldsymbol{M}\boldsymbol{G'G}) + \sigma_M^{-2}\Delta\boldsymbol{M} = \sigma_D^{-2}(\boldsymbol{G'X} + \boldsymbol{YG})$$

This matrix equation can be rearranged to:

$$(\boldsymbol{G'G} + \epsilon^2\boldsymbol{I})\Delta\boldsymbol{M} + \Delta\boldsymbol{M}\boldsymbol{G'G} = \boldsymbol{G'X} + \boldsymbol{YG} \quad (3)$$

Equation (2) is an equation in $\Delta\boldsymbol{M}$ of the form

$$\boldsymbol{A}\Delta\boldsymbol{M} + \Delta\boldsymbol{M}\boldsymbol{B} = \boldsymbol{C}$$

for matrices $\boldsymbol{A}, \boldsymbol{B}$ and $\boldsymbol{C}$ with appropriate dimensions. This is a so-called *Sylvester Equation* for which no simple closed-form solution has been found. However, a stable numerical solution is available. See, e.g., De Terán et al. (2016).

NUMERICAL METHOD

To demonstrate and test our method, we created a synthetic test example. This numerical experiment aims to investigate if our method and algorithm is able to reconstruct a known, controlled area. From a set of real topographic LOLA data (which in this test plays the role as

the "unknown" high-resolution map), we computationally created a photographic image and computed, by simple downscaling, a low-resolution version of the topographic LOLA map. The synthetic photo was computed by subjecting the artificial high-resolution topography to illumination with a chosen illumination angle.

On Figure 1, we see the real LOLA topographic data from and area on the Moon located around $25{,}41\,°N$ and $2{,}83\,°E$ from SLDEM2015 Planetary Data System LOLA data node: (http://imbrium.mit.edu/EXTRAS/SLDEM2015).

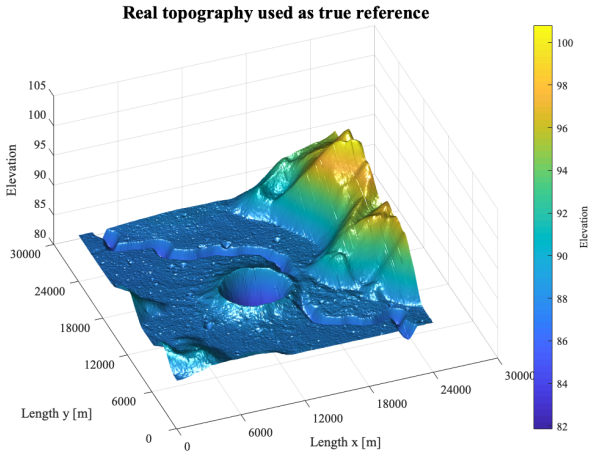

Figure 1 – Topography of the area used for the numerical example from LOLA (NASA/PDS/MIT).

From this image we used a down-sampling operator downscale it 40 times from the original one and create a low-resolution topography (Figure 2).

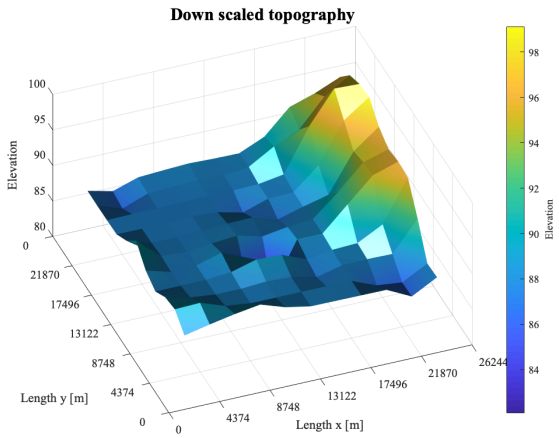

Figure 2 – Synthetic low-resolution topography, 40 times down-scaled.

To be able to perform inversion, we transformed the LOLA low resolution topographic data into a smooth, upscaled map with the same pixel size as the photographic image (see Figure 3).

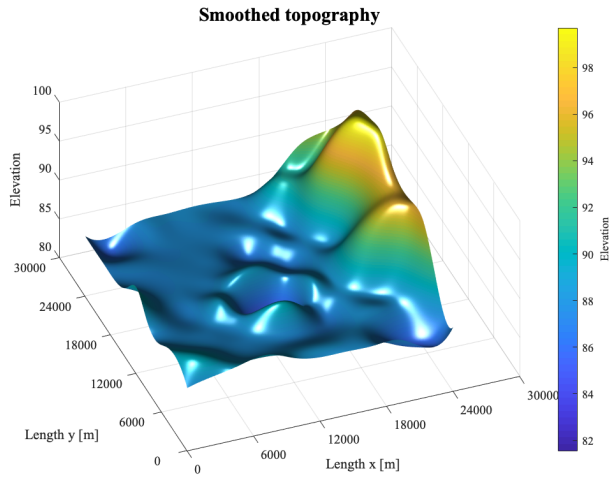

Figure 3– Smoothed low resolution topography with high number of pixels.

We now created an artificial photography (Figure 4) from Figure 1 with illumination angles: azimuth = $-20°$ (where West = $0°$, and North = $-90°$), elevation of sun = $15°$ (angle of sun over horizon).

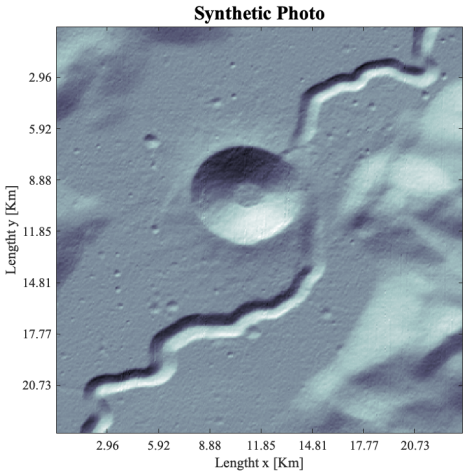

Figure 4– Synthetic optical imagery with incidence angle of 65° and azimuth of 160° degrees.

Then the gradients in North-South and East-West directions were computed (Figure 5):

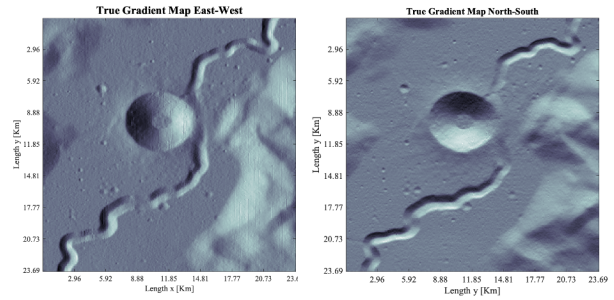

Figure 5 – Gradients of the synthetic photo image.

from the illumination of the artificial photographic data. The direction of the light determines which one if the components, N-S or E-W, of the gradient will be more pertinent for the calculations. Gradients in the image, with solar illumination angles close to parallel with the surface will be better determined than those with a near-90° illumination.

As shown on Figure 6, the influence of the gradients will be 74% for the North-South direction and 26% for the East-West direction. In some cases there can be a shadow coming from the Sub Solar Azimuth angle (Figure 6a). The incidence angle represents the angle in relation to the surface (Figure 6b).

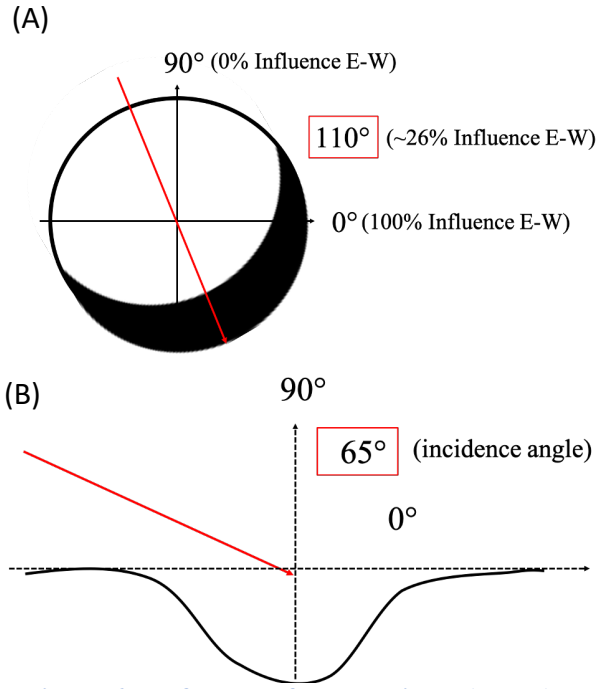

Figure 6 – Influence of the gradients (slopes) depending on the incidence angle. (A) Top figure shows the definition of the azimuth angle. (B) Bottom figure shows the incidence angle.

Performing the least-squares inversion, we computed the high-resolution topography from the synthetic photo, using the down-sampled low-resolution topography as a constraint. the result can be seen on Figure 7.

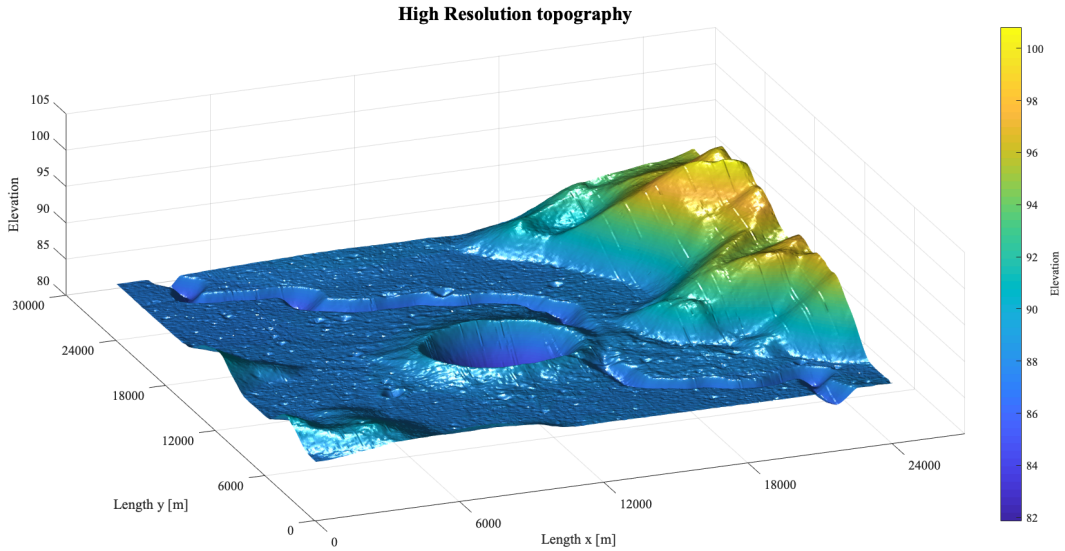

Figure 7 – Computed synthetic high-resolution topography.

To verify the precision, Figure 8 shows a cross-section of the initial high-resolution reference (Figure 1) with the computed topography from the inversion (Figure 7).

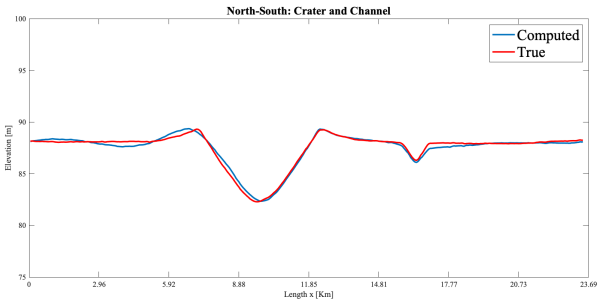

Figure 8 – Cross-section of the initial and computed terrain maps.

It is observed that the computed topography is very close the to the initial test example. From the low-resolution elevation map, it was not possible to observe the finer details seen on the photo image. These details were retrieved after inversion is performed, as shown in the reconstructed high-resolution elevation map.

RESULTS

We use now the real imagery data of an area centred around $22{,}23\,^{\circ}N$ and $29{,}61\,^{\circ}E$, in the Region of Interest (ROI) of the Apollo 15 landing site. The area ranges approximately $5881m \times 5881m$.

The optical image data covering this area was provided by LROC, observations M1249338893R, M1249338893L, M1249345927R, M1249345927L, combined by Klem, S. et all (2014) (Figure 9) with a resolution of 0,9 m per pixel.

On Figure 9, the lava channels, craters and other surface features are shown illuminated with sun light with an incidence angle of $65{,}88\,^{\circ}$ and an azimuth angle of $81{,}76\,^{\circ}$.

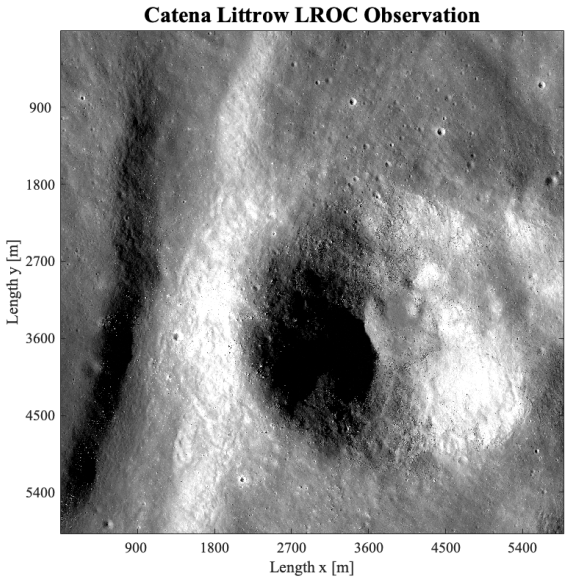

Figure 9 – Lunar landforms with illumination and incidence angle of 65,88° from LROC (NASA/GSFC/Arizona State University).

The topographic map of the area can be seen on Figure 10. Acquired by *LOLA, 2015,* the resolution is 512 pixels per degree, corresponding to $59{,}225m$ per pixel.

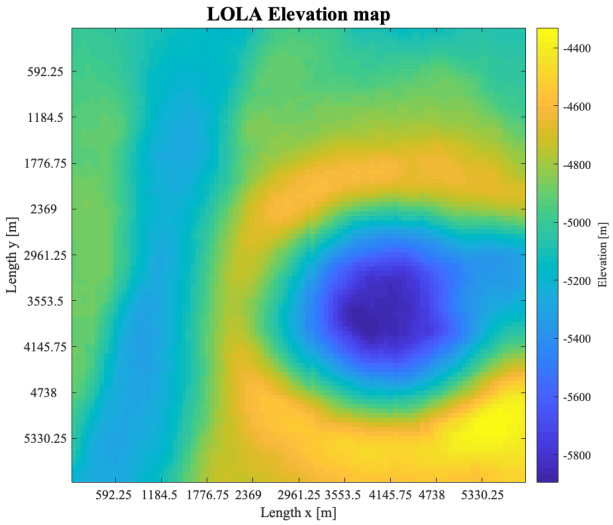

Figure 10 – Topography of the area covering the Catena Littrow ROI from LOLA (NASA/PDS/MIT).

We calculated the gradients from the photo showing the influence of light on the surface structures. The influence of light is 47% in the East-West direction and 53% in the North-South direction.

To be able to perform inversion, a smoothed version of the low-resolution LOLA data (Figure 10) was computed, generating a same resolution image but with a larger number of points.

Small scaled features are revealed on Figure 11. Craters and other landforms can be observed from the reconstructed up-scale elevation map.

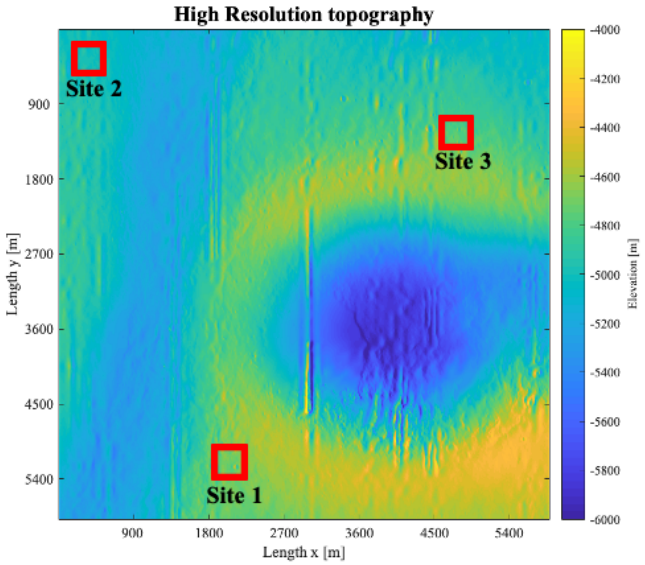

Figure 11 – Computed high resolution elevation map with three selected sites.

On Figure 11 with the high resolution topography of a $5.8\,\text{km} \times 5.8\,\text{km}$ area, we selected 3 sites to better show detailed surface features and landforms.

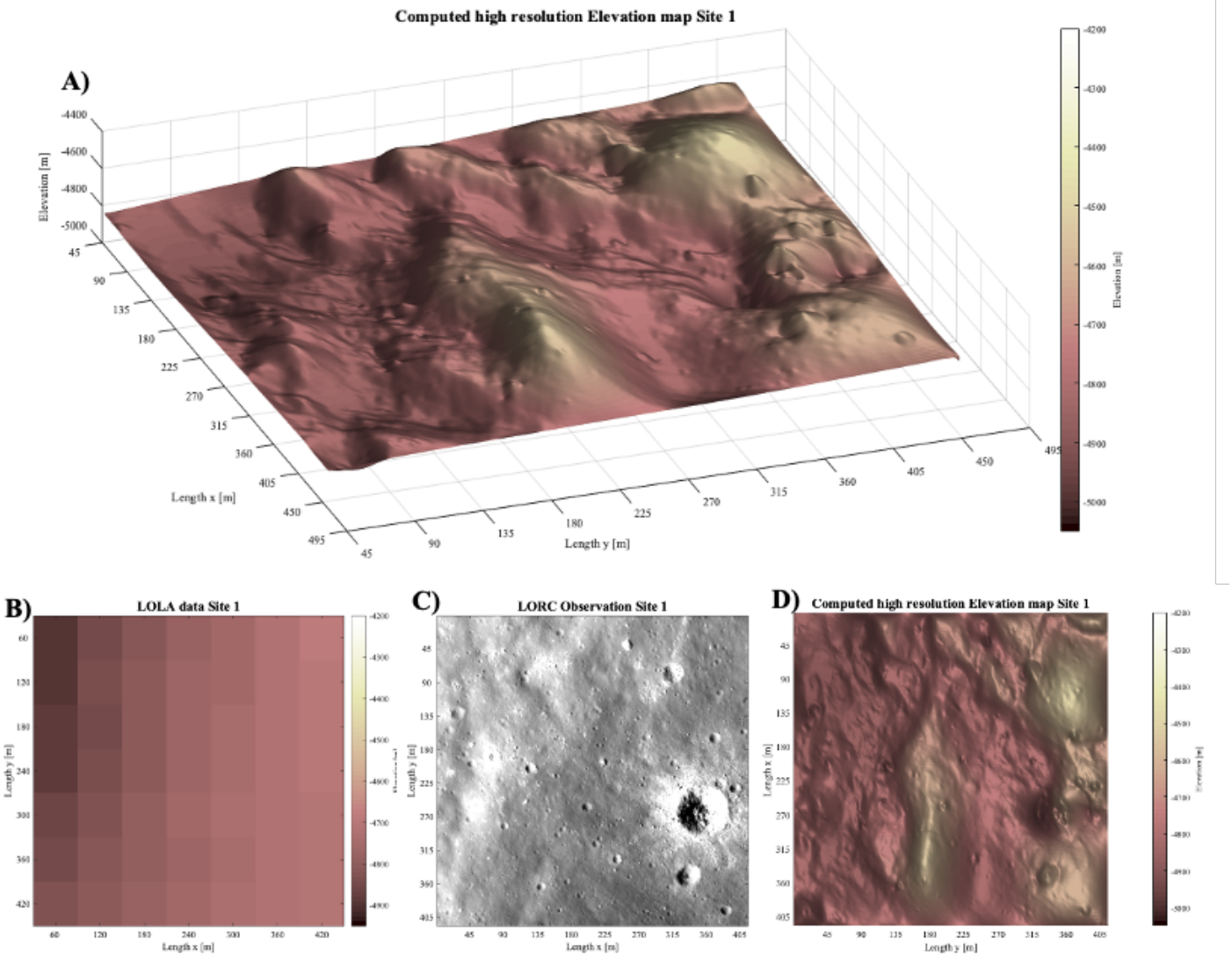

Figure 12 – (A) Computed high-resolution topographic map of Site 1, (B) LOLA data, (C) LROC Observation of Site 1 and (D) Computed high resolution elevation map of Site 1.

Site 1 is shown on Figure 12 alongside with the corresponding LOLA data of the area. On Figure 12B we cannot see any of the landforms observed on the photo from LROC. These features were retrieved, and the topography is shown on Figure 12A and Figure 12D in an area of $\sim 400m \; x \; 400m$.

Site 2 shows the surface from a different, detailed area of $\sim 450m \; x \; 450m$ (Figure 13). Figure 13A presents small craters and a significant change in elevation. Small craters can also be seen on the LROC observation of the corresponding area on Figure 13B and an even smaller detailed area was selected to show the smallest surface features that the high resolution elevation map can detect (Figure 14).

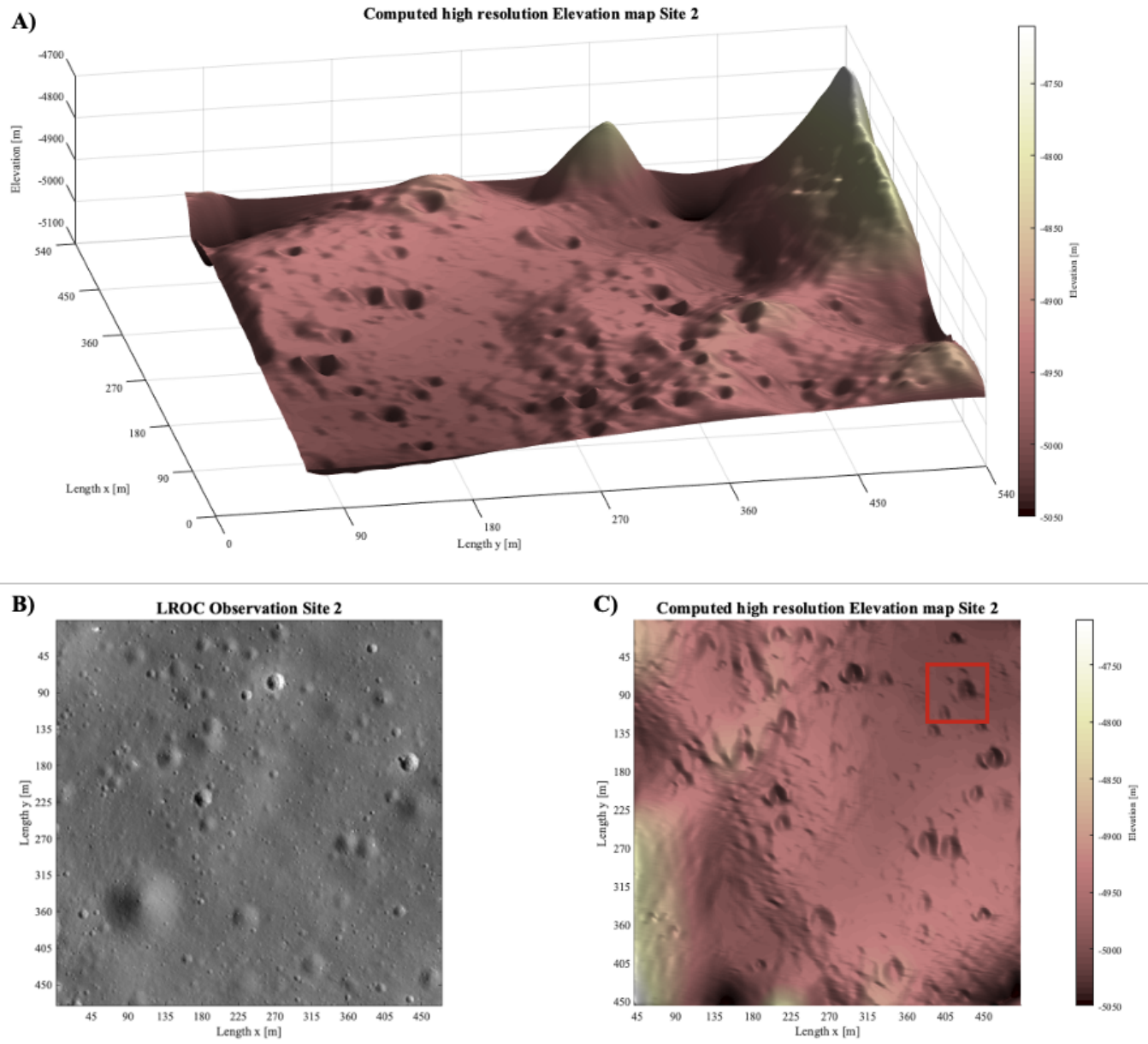

Figure 13 – (A) Computed high-resolution topographic map of Site 2, (B) LROC photo of Site 2, and (C) Computed high resolution elevation map of Site 2.

The next chosen area is site 3 shown on Figure 14, representing an area of $\sim 500m \times 500m$. Site 3 shows significant changes in elevation, and craters in small, medium and large size.

Another detail is even smaller and selected form Site 3, and can be seen on Figure 15.

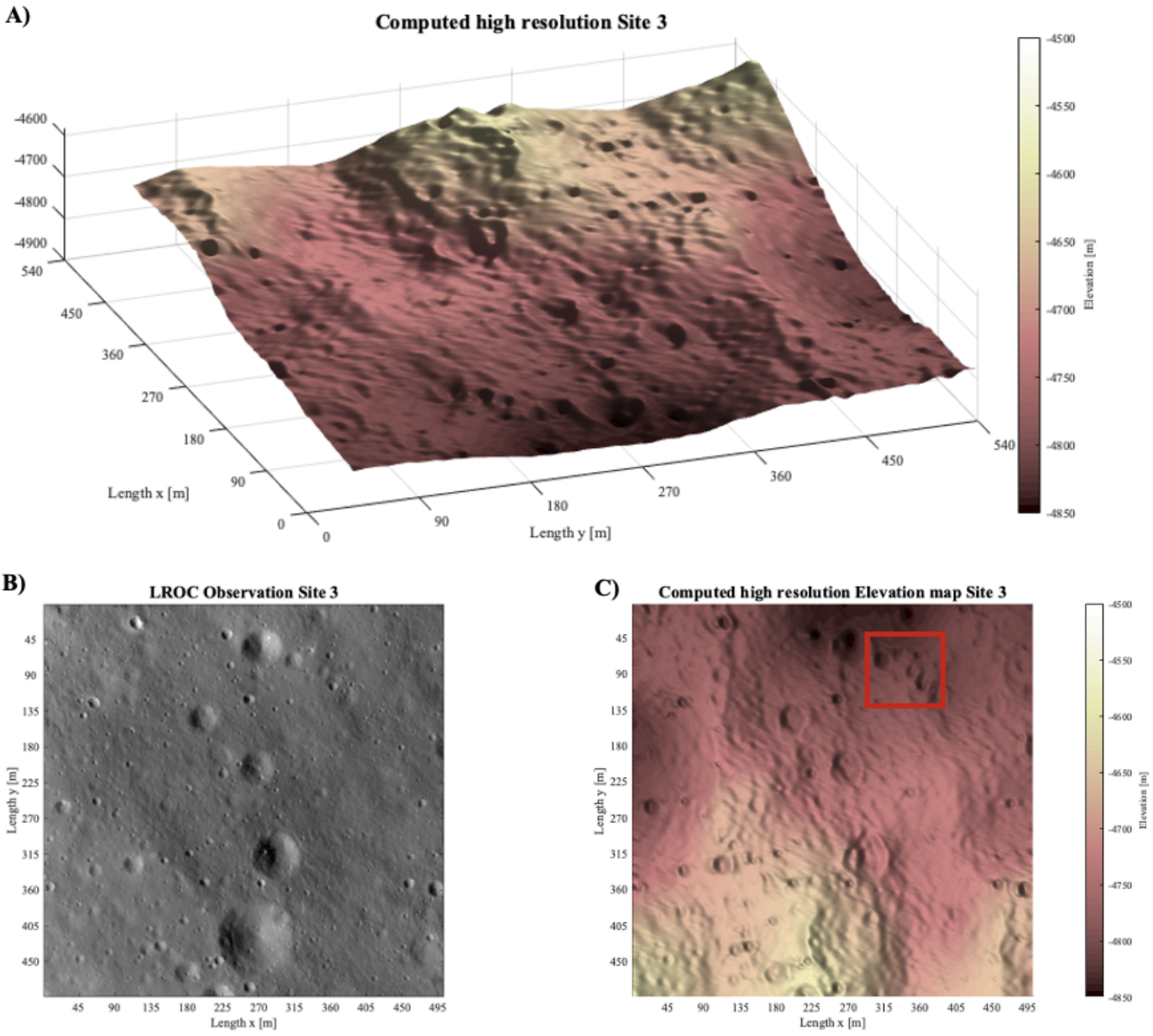

Figure 14 – (A) Computed high-resolution topographic map of Site 1, (B) LROC observation of Site 1, and (C) Computed high resolution elevation map.

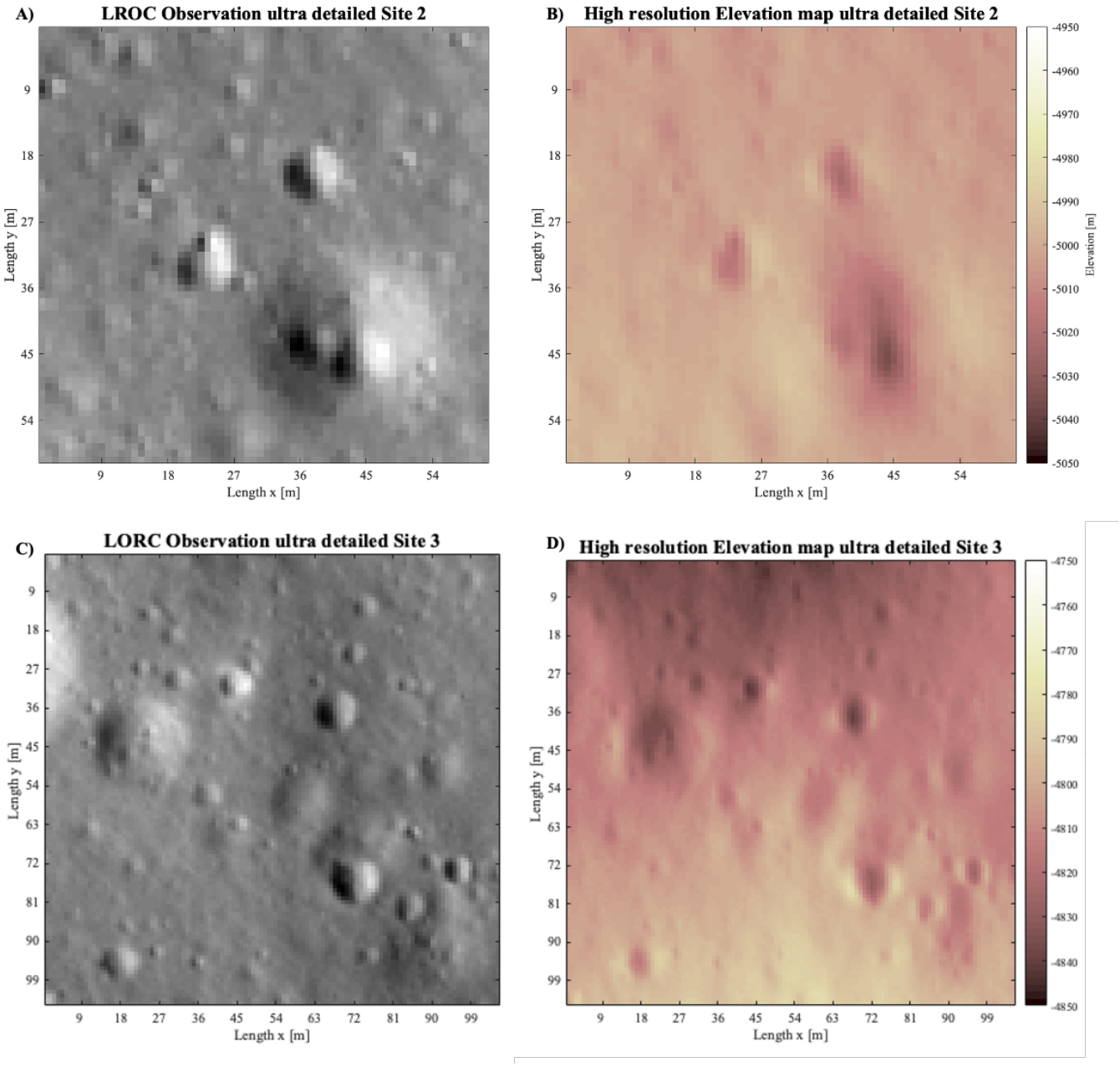

Figure 15 – (A) LROC observation of detail in Site 2, (B) Computed high-resolution topographic map of detail in Site 2, (C) LROC observation of detail in Site 3 and (D) Computed high-resolution topographic map of detail in Site 3.

Figure 15 shows the two detailed areas marked on Figure 13C and Figure 14C.

The topography of small craters with diameters ranging from $\sim 25m$ down to $\sim 3m$, can easily be observed on Figure 15.

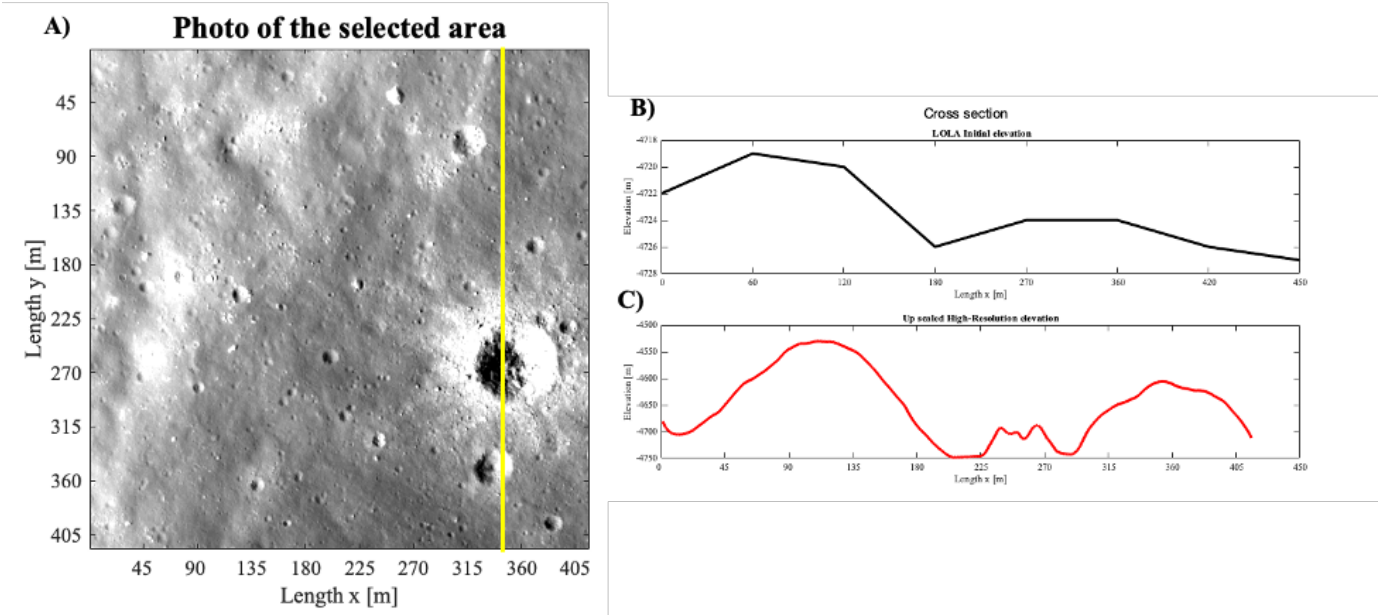

Figure 16 – (A) Cross section of the area, (B) Elevation data from LOLA, C) Computed high-resolution elevation.

From the detailed area shown on Figure 12, we show (Figure 16) a cross-section comparing the initial LOLA data, the smoothed upscaled low resolution topography map and our computed high-resolution elevations.

The high-resolution cross-section (Figure 16C) shows the elevations of small craters, which are unseen from the initial LOLA resolution (Figure 16B), where the elevation is averaged, and the terrain features are not clearly represented.

The precision of positions in the elevation are influenced by the numerical assumptions we made. We assumed constant albedo everywhere, so all the variation in the illumination of the surface is assumed to be from the slopes. This will add uncertainties in positions of the elevation map.

Assuming a Gaussian uncertainty on the albedo with a standard deviation of 10%, we estimated the spatial distribution of the uncertainties in elevation. The estimation was done with a Monte Carlo method where a large number of realizations of the solution were computed with different albedo perturbations. The mean of the perturbations was 0 and the standard deviation was 10% of the mean albedo, which was set to 0.12. The albedo variations were spatially independent, Gaussian values. Figure 17 shows an uncertainty map of the topography, calculated form 100 albedo realizations.

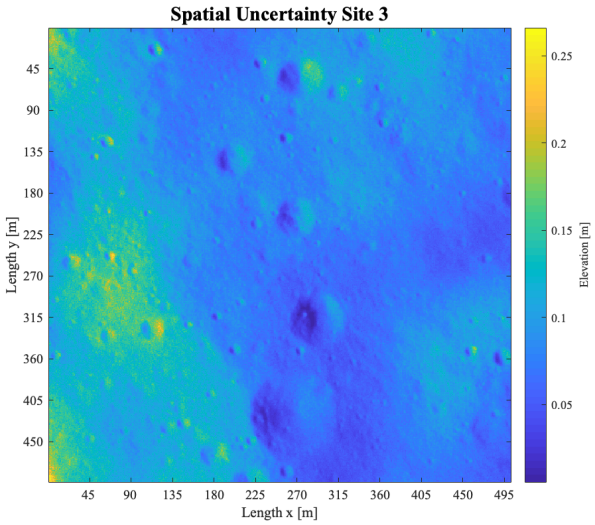

Figure 17 – Spatial uncertainty map of the elevation for the Site 3.

It is seen that albedo errors result in uncertainties range up to ~0.26 m and are, as expected, higher where the illumination is near-perpendicular to the terrain.

However, the most significant uncertainties in our results are likely to originate from systematic errors due to limitations in the illumination. Working with a single illumination, as we have done in this study, limits the input information to the algorithm and will inevitably result in some distortion of the result.

DISCUSSION

In the high resolution elevation maps from real-data (Figure 7 and Figure 11) we can observe N-S going stripes that go across the area. This is from errors in the data acquisition creating offsets in the LOLA profiles (Barker, M.K. et al. (2015)). During the inversion, they are amplified, as our method interprets them as terrain features. However, they are not seen in, or influencing, the smaller areas from the selected Sites 1, 2 and 3.

As we consider illumination from only one angle in this study, some anisotropy is in some cases distorting the crater rims, amplifying their height around the direction of the illumination. This is an effect that starts to appear in geological features of approximately 3 metres in diameter and can be reduced by adding photographic data from several illumination angles.

In the initial resolution provided by LOLA data, it is only possible to observe large geological features of the scale of hundreds of metres, as one pixel has ~60 metres. Our up-scaled and high-resolution results offer a way to detect structures of the size of small craters and lava pit entrances.

Combining our method with improved-resolution LOLA data, as presented by Barker et al. (2021), can potentially produce high-resolution topography maps of a very high quality.

CONCLUSION

In this study, we developed a computational method that uses optical images from LRO camera (LROC) constrained by topographic data from the Lunar Orbiter Laser Altimeter (LOLA) onboard the Lunar Reconnaissance Orbiter (LRO) in order to create an upscaled Digital Elevation Model (DEM) of lunar landforms.

In our study we used the original LOLA altimeter data with a resolution of 512 pixels per degree, which provides a ~60 metres per pixel resolution. These data were used as a constraint in our inverse problem formulation to compute a final topographic map from photos with a resolution of 0,9 metres per pixel. The resulting topographic map was upscaled to the same, high resolution.

In our formulation, we assumed constant albedo, therefore, the brightness is assumed to be related directly to the slopes. For this reason, we also computed the spatial uncertainty resulting from 10% albedo variations. This uncertainty was computed to be up to 0.26 metres.

The results provide a high-resolution and upscaled DEM, being able to map geological structures down to a scale of around 3 metres. Hence, our formulation provides not only a high resolution imagery but also a new technique to remove shades from features such as caves or lava pit entrances. The method also offers an alternative to study in greater details regions of interest without the need of expensive engineering feats.

Future perspectives of this work are to improve the capabilities of this method to map formations of more sophisticated and challenging shapes and smaller-scaled sizes, as well as using the colour information of photos to study rock-physical properties of planets. Photos with several illumination angles and use of improved LOLA data with higher resolution (Barker et al., 2021) are obvious sources of information to generate terrain maps of hitherto unseen detail.

APPENDIX

Minimization of a General Misfit

Consider minimization of the general expression with respect to the matrix $\boldsymbol{\mathcal{M}}$:

$$E_D(\boldsymbol{\mathcal{M}}) = \|\boldsymbol{G\mathcal{M}F'} - \boldsymbol{D}\|^2 = \sum_i \sum_j \left[D_{ij} - \sum_k \sum_l G_{ik}\mathcal{M}_{kl}F_{jl} \right] \left[D_{ij} - \sum_m \sum_n G_{im}\mathcal{M}_{mn}F_{jn} \right]$$

where G, F and D are matrices. Multiplying the square brackets and reversing the order of the summations gives

$$E_D(\boldsymbol{\mathcal{M}}) = \sum_k \sum_l \sum_m \sum_n \mathcal{M}_{kl}\,\mathcal{M}_{mn} \sum_i \sum_j G_{ik}F_{jl}G_{im}F_{jn} - 2\sum_m \sum_n \mathcal{M}_{mn} \sum_i \sum_j D_{ij}G_{im}F_{jn} + \sum_i \sum_j D_{ij}D_{ij}$$

We can now compute the derivatives $\partial E_D / \partial \mathcal{M}_{pq}$ term by term:

$$\frac{\partial}{\partial M_{pq}} \sum_k \sum_l \sum_m \sum_n \mathcal{M}_{kl}\,\mathcal{M}_{mn} \sum_i \sum_j G_{ik}F_{jl}G_{im}F_{jn} = \sum_k \sum_l \sum_m \sum_n \left[\delta_{(kl)(pq)}\mathcal{M}_{mn} + \mathcal{M}_{kl}\delta_{(mn)(pq)} \right] \sum_i \sum_j G_{ik}F_{jl}G_{im}F_{jn}$$

$$= \sum_k \sum_l \left(\delta_{(kl)(pq)} \sum_m \sum_n \mathcal{M}_{mn} \sum_i \sum_j G_{ik} F_{jl} G_{im} F_{jn} \right.$$

$$\left. + \mathcal{M}_{kl} \sum_m \sum_n \delta_{(mn)(pq)} \sum_i \sum_j G_{ik} F_{jl} G_{im} F_{jn} \right)$$

$$=$$

$$= 2 \sum_m \sum_n \mathcal{M}_{mn} \sum_i \sum_j G_{ip} F_{jq} G_{im} F_{jn}$$

and

$$\frac{\partial}{\partial M_{pq}} \left(-2 \sum_m \sum_n \mathcal{M}_{mn} \sum_i \sum_j D_{ij} G_{im} F_{jn} \right)$$

$$= -2 \sum_m \sum_n \delta_{(mn)(pq)} \sum_i \sum_j D_{ij} G_{im} F_{jn}$$

$$= -2 \sum_i \sum_j D_{ij} G_{ip} F_{jq}$$

and

$$\frac{\partial}{\partial \mathcal{M}_{pq}} \left(\sum_i \sum_j D_{ij} D_{ij} \right) = 0.$$

All in all, we have:

$$\frac{\partial E_D}{\partial \mathcal{M}_{pq}} = 2 \sum_m \sum_n \mathcal{M}_{mn} \sum_i \sum_j G_{ip} F_{jq} G_{im} F_{jn} - 2 \sum_i \sum_j D_{ij} G_{ip} F_{jq}$$

$$= 2 \sum_m \sum_n \sum_i \sum_j G_{ip} G_{im} \mathcal{M}_{mn} F_{jn} F_{jq} - 2 \sum_i \sum_j G_{ip} D_{ij} F_{jq}$$

$$= 2 \sum_m \sum_n \sum_i \sum_j G'_{pi} G_{im} \mathcal{M}_{mn} F'_{nj} F_{jq} - 2 \sum_i \sum_j G'_{pi} D_{ij} F_{jq}$$

or, in matrix notation,

$$\left\{ \frac{\partial E_D}{\partial \mathcal{M}_{pq}} \right\} = 2\boldsymbol{G'GMF'F} - 2\boldsymbol{G'DF} \qquad (3)$$

REFERENCES

Barker, M.K., E. Mazarico, G.A. Neumann, M.T. Zuber, J. Haruyama, and D.E. Smith. “A New Lunar Digital Elevation Model from the Lunar Orbiter Laser Altimeter and SELENE Terrain Camera.” Icarus 273 (July 2016): 346–355.

Barker, M. K., Mazarico, E., Neumann, G. A., Smith, D. E., Zuber, M. T., & Head, J. W. (2021). Improved LOLA elevation maps for south pole landing sites: Error estimates and their impact on illumination conditions. *Planetary and Space Science*, *203*, 105119.

De Terán, F., Iannazzo, B., Poloni, F., Robol, L., 2017, Solvability and uniqueness criteria for generalized Sylvester-type equations. ArXiv.org: 10.1016/j.laa.2017.10.018

Haruyama, J. et al., 2009. Possible lunar lava tube skylight observed by SELENE cameras. In: Advancing Space and Earth Sciences (AGU), Vol.36, Issue 21. DOI: doi.org/10.1029/2009GL040635

Haruyama, J. et al., 2012. Lunar global digital terrain model dataset produced from SELENE (Kaguya) terrain camera stereo observations. In: Lunar and Planetary Science Conference, p. 1200.

Haruyama, J. et al., 2014. Data products of SELENE (Kaguya) Terrain Camera for future lunar missions. In: Lunar and Planetary Science Conference, p. 1304.

Johnson, A., et al., 2010. An integrated traverse planner and analysis tool for plane- tary exploration. Am. Inst. Aeronaut. Astronaut. doi:10.2514/6.2010-8829, http: //dx.doi.org/10.2514/6.2010- 8829.

Kaku, T., Haruyama, J., Miyake, W., Kumamoto, A., Ishiyama, K., Nishibori, T., ... Howell, K. C. (2017). Detection of intact lava tubes at Marius Hills on the Moon by SELENE (Kaguya) lunar radar sounder. Geophysical Research Letters, 44, 10,155–10,161. https://doi.org/ 10.1002/2017GL074998

Klem, S. M., Henriksen, M. R., Stopar, J., Boyd, A., & Robinson, M. S. (2014). Controlled LROC Narrow Angle Camera High Resolution Mosaics. In *Lunar and Planetary Science Conference* (Vol. 45, abstract #2885).

Mosegaard, K., and Hansen, T. M., 2016. Inverse Methods: Problem formulation and Probabilistic Solution. Chapter 2, Integrated Imaging of the Earth, Theory and Applications. AGU, ISBN: 978-1-118-92905-6.

Mosegaard, K., and Tarantola, A., 1995. Monte Carlo sampling of solutions to inverse problems: Journal of Geophysical Research 100, B7, pp. 12431-12447.

NASA Surveyor Project Final Report. NASA Jet Propulsion Laboratory. (1968).

SLDEM2015 Planetary Data System LOLA data node:(http://imbrium.mit.edu/EXTRAS/ SLDEM2015).

Smith, D.E., et al., 1997. Topography of the Moon from the Clementine LIDAR. J. Geo- phys. Res. 102, 1591. doi:10.1029/96JE02940.

Smith, D.E., et al., 2010. Initial observations from the Lunar Orbiter Laser Altimeter (LOLA). Geophys. Res. Lett. 37, 18204. doi:10.1029/2010GL043751.

Smith, D.E., et al., 2010. The Lunar Orbiter Laser Altimeter investigation on the Lu- nar Reconnaissance Orbiter Mission. Space Sci. Rev. 150, 209–241. doi:10.1007/ s11214- 009-9512- y.

Tarantola, A., and B. Valette, 1982, Inverse problems = quest for information: Journal of Geophysics Research, 50, 150-170.

Tarantola, A., Inverse Problem Theory and Methods for Model Parameter Estimation. Siam, Philadelphia, 2005.

William Whittaker (2012), Technologies Enabling Exploration of Skylights, Lava Tubes

and Caves, NASA Innovative Advanced Concepts (NIAC) Phase I.